Failure Envelopes for Combined Loading of Skirted Foundations in Layered Deposits

Barari, Amin; Ghaseminejad, Vali; Ibsen, Lars Bo

Published in:
Journal of Waterway, Port, Coastal, and Ocean Engineering

DOI (link to publication from Publisher):
10.1061/(ASCE)WW.1943-5460.0000639

Publication date:
2021

Document Version
Publisher's PDF, also known as Version of record

Failure Envelopes for Combined Loading of Skirted Foundations in Layered Deposits

Amin Barari, M.ASCE[1]; Vali Ghaseminejad[2]; and Lars Bo Ibsen, M.ASCE[3]

Abstract: A robust and integrated interpretation of soil data from field investigations can provide valuable insights into the important role of soil deterioration following the installation of suction caissons. Therefore, a field experiment was conducted at a site in Frederikshavn to simulate laterally loaded suction caisson in a layered soil profile. The experiment was performed to validate our modeling approach and to systematically analyze the predictive capabilities of three classes of numerical predictions (Classes A, A1, and C). The Class A1 prediction focused primarily on the trajectory of the rotation center and the capacity of existing failure criteria to predict the bearing strength of shallow foundations under combined loading, despite differences in stress conditions, foundation geometries, and soil weakening due to the installation effect. On the other hand, the Class A prediction was carried out based on wished-in-place conditions. Failure envelopes within the Class C predictions were adopted to be scaled by the pure bearing capacities (given by intersections with the axes). Subsequently, the appropriateness of identical envelopes was examined here by employing three-dimensional finite-element analyses in the presence of the parabolic variations in soil stiffness with depth. An alternative macroelement model of varying failure surface parameters was also represented, which enables the bearing capacity of skirted foundations to be predicted for a wide range of embedment ratios and sand strength inhomogeneities. **DOI: 10.1061/(ASCE)WW.1943-5460.0000639**.

Author keywords: Calibration; Suction bucket foundation; HSsmall model; Failure envelope; Failure mechanism.

Introduction

Despite the 2011 Fukushima Daiichi nuclear power plant disaster, the number of large-scale offshore wind farms under construction is growing, in accordance with the 21st meeting of the Conference of Parties (COP 21). Fig. 1 illustrates the distribution of offshore wind farms in Europe (Bhattacharya 2019). In addition, pioneering efforts in offshore wind harvesting are underway with farms being constructed in China, Taiwan, South Korea, and Japan (Bhattacharya 2019).

Monopiles and gravity-based foundations are currently being considered or deployed for water depths of approximately 30 m. More recently, suction bucket foundations have been designated for installation in water depths of 20–25 m at the Dogger Bank. These foundations are also under special consideration for deployment at water depths up to 40 m. To withstand severe loading due to wave, current, wind forces, and superstructure loads and to improve the fixity of offshore facilities, the foundations of offshore structures are fitted with circumference steel skirts. Soil plugs are confined inside these skirts, which penetrate the seabed and apply suction until full contact with underlying soil is achieved.

Skirted foundations are increasingly being incorporated into the design of offshore wind turbine structures and facilities to help them withstand combined vertical (V), horizontal (H), and moment (M) loading conditions. Skirted foundations have also attracted considerable attention for offshore wind energy converters based on their ease of installation, cost effectiveness, and avoidance of noise emission compared with deep footings such as monopiles and piled foundations (Barari and Ibsen 2017; Ibsen et al. 2015).

To date, classical design methods and determinations of individual modification factors have not been able to accurately consider interactions of effective parameters in bearing capacity expressions. Thus, the conventional bearing capacity of a foundation under combined vertical, horizontal, and moment loads is often replaced and expressed by the planes of H:V, H:M, and M:V interaction envelopes and sometimes in three-dimensional (3D) space through a failure surface. Moreover, the capacity of bucket foundations has been expressed by using a failure envelope approach. In the interaction diagrams of failure envelopes, the effects of foundation geometry, horizontal load eccentricity, and various soil conditions are all important factors.

Investigations into the bearing capacity of shallow foundations have particularly included the work-hardening plasticity theory (Cassidy et al. 2002; Gottardi et al. 1999; Bienen et al. 2012). The theories developed to date can provide a suitable simulation of load–deformation responses of shallow footings. In particular, the bearing capacity of suction caissons under general loading is of particular interest in the field of offshore renewable energy. Previous studies on suction caissons have been limited to laboratory model tests (Barari and Ibsen 2012; Zhu et al. 2019), field tests (Houlsby et al. 2005), and numerical studies (Gourvenec 2008; Achmus et al. 2013; Vulpe et al. 2014; Gerolymos et al. 2012).

Background

Macroelement models take into account an entire soil–foundation system, with a single element located beneath the system, representing nonlinear soil–structure interactions. The model has the

[1]Associate Professor, Dept. of the Built Environment, Aalborg Univ., Thomas Manns Vej 23, 9220 Aalborg Ø, Denmark (corresponding author). Email: abar@build.aau.dk

[2]Assistant Professor, Dept. of Civil Engineering, Azad Univ., Nowshahr Branch, Nowshahr 46511–41433, Iran. Email: vghaseminejad@gmail.com

[3]Professor, Dept. of the Built Environment, Aalborg Univ., Thomas Manns Vej 23, 9220 Aalborg Ø, Denmark. Email: lbi@build.aau.dk

Note. This manuscript was submitted on July 7, 2020; approved on February 4, 2021; published online on March 24, 2021. Discussion period open until August 24, 2021; separate discussions must be submitted for individual papers. This paper is part of the ***Journal of Waterway, Port, Coastal, and Ocean Engineering***, © ASCE, ISSN 0733-950X.

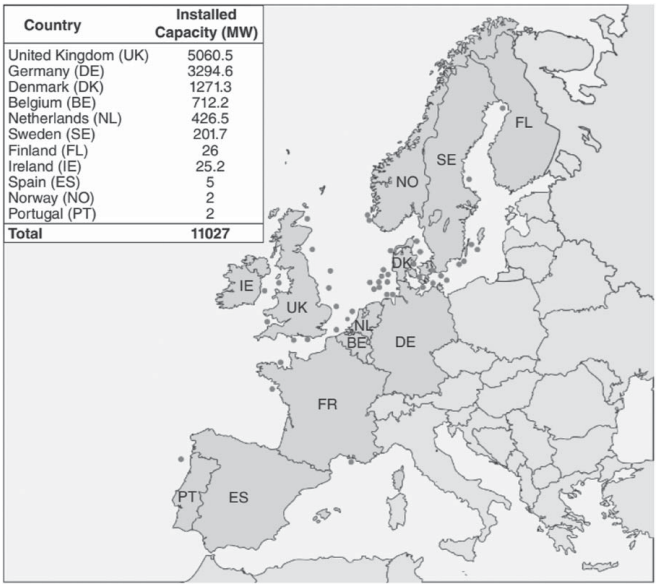

Fig. 1. Distribution of offshore wind farms in Europe.

following substantial advantages as described by Gerolymos et al. (2012):

1. Sophisticated 3D nonlinear soil–structure interaction (SSI) analyses can be omitted given the analytical feature of the model.
2. A unified mathematical framework can be developed that would govern foundation response prior to, and upon, failure.

Accordingly, Model C was adopted by Gottardi and Houlsby (1995). This model provides a unified basis for representing the performance of rough, rigid, circular footings resting on dry, dense, Yellow Leighton Buzzard sand under fully drained conditions. The model is thoroughly elaborated in Gottardi et al. (1999) and Cassidy et al. (2002).

Ibsen et al. (2014a, b) further conducted a large set of combined loading model tests on bucket foundations in dense sand. They found that the response of a bucket foundation cannot be exclusively represented by a yield surface with an apex at its origin. Rather, a negative vertical load arising from a tension capacity is needed (Larsen et al. 2013; Ibsen et al. 2014a, b).

In original Model C, the yield surface is assumed to be constant in shape (Gottardi et al. 1999). Subsequently, Ibsen et al. (2014a, b) demonstrated that the shape of the failure envelopes for circular surfaces and skirted footings changes according to the level of the vertical load (i.e., $\upsilon = V/V_0$ or V/V_{ult}):

$$f = \left(\frac{H}{h_0 V}\right)^2 + \left(\frac{M}{m_0 DV}\right)^2 - 2a\left(\frac{H}{h_0 V}\right)\left(\frac{M}{m_0 DV}\right) - F(V,\ V_t,\ \upsilon) = 0 \tag{1}$$

where f = yield surface; H and V = horizontal and vertical loads, respectively; M = moment capacity; V_0 or V_{ult} = bearing capacity under pure vertical load; V_t = tensile capacity; h_0 and m_0 = parameters that determine the size of the yield surface at the widest section of the surface along the V-axis; D = foundation diameter; and a = eccentricity parameter.

Changes in the shape of the yield surface with increasing embedment ratio and level of vertical load may mathematically be represented in a normalized form defined in Eq. (2). Expansion of the yield surface is clearly evident in Fig. 2. The normalized variables show higher disparity depending on the embedment ratio outside the first and third quadrants, which are relevant to offshore wind

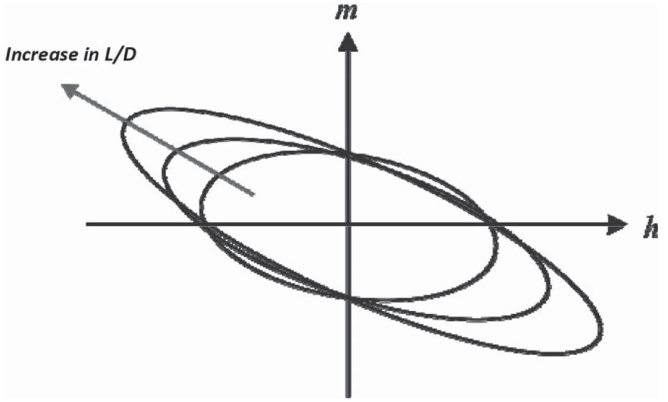

Fig. 2. Normalized yield surface and its expansion with changes in embedment ratios (L/D, where L and D = skirt length and foundation diameter, respectively).

turbines:

$$\begin{cases} h = \dfrac{H}{V_{peak} h_0 \beta_{12} \upsilon^{\beta_1} (1-\upsilon)^{\beta_2}} \\ m = \dfrac{M}{D V_{peak} m_0 \beta_{12} \upsilon^{\beta_1} (1-\upsilon)^{\beta_2}} \end{cases} \tag{2}$$

where β_1 and β_2 = curvature factors (Cassidy 1999) that allow adjustments to the shape of the yield surface. Parameter β_{12} can be determined from the following equation:

$$\beta_{12} = \left(\frac{(\beta_1+\beta_2)^{\beta_1+\beta_2}}{\beta_1^{\beta_1}\beta_2^{\beta_2}}\right)^2 \tag{3}$$

This paper focused on the results of Class A and Class C predictions because they are promising in regard to establishing algebraic expressions for the failure envelopes of suction caissons and for establishing unbiased capabilities and limitations of cone penetration test (CPT)-based soil strength parameters in finite-element analysis (FEA). The classes of prediction and validation, A, A1, and C, are differentiated as follows. The Class A predictions elaborate a consistent 3D numerical model for laterally loaded suction bucket foundations installed at the Frederikshavn test site based on the available ground information. Performance is predicted according to intact soil properties obtained prior to caisson installation. Class A1 validation is performed after the installation of caissons, in combination with scrutinizing macroelement models and their applicability to multilayered soils. Finally, the Class C prediction is presented to investigate the effects of bucket foundation geometry, relative strength heterogeneity, load eccentricity on the shape of failure envelopes, and soil deformation mechanisms occurring at failure. Of particular interest is whether an internal mechanism can be developed within the soil plug of offshore skirted foundations that can reduce the mobilized capacity.

The caisson support structure was considered as a rigid body with a load reference point (RP) located at the skirt top level along the centerline of the bucket. The sign conventions for displacements and loads used in this study are provided in Fig. 3.

Field Test in Frederikshavn: Basis for Calibration

A test program on a medium-scale bucket foundation was performed within the period of this work. The foundation was loaded until failure and was located in a natural sand deposit. The test

program included installation tests and combined loading of the bucket foundation upon failure. To the best of our knowledge, the present test program is unique and no corresponding loading tests have been carried out.

A test site in Frederikshavn, in the northern part of Jutland, was established (Fig. 4). The test site includes a bucket foundation located in a dammed area near the sea (Fig. 4). Both the skirt length and diameter of the bucket foundation are 2 m, resulting in an embedment ratio (L/D) of 1. The thickness of the skirt is 12 mm. Seven loading tests were performed at this test site. The tests were conducted with varying heights of impact and a small vertical load compared to the vertical bearing capacity of the foundation [i.e., low $\upsilon = (V/V_{ult})$].

During installation and loading, an extensive measurement program was established. Briefly, prior to each loading test, the bucket foundation was installed by applying suction to the inside of the bucket. After installation, a three-legged lattice tower from an old wind turbine was bolted to the bucket lid (Fig. 5). Each leg was bolted to the bucket through a load cell.

After being completely assembled, the bucket foundation was loaded in the same manner as offshore wind turbine foundations are loaded. Briefly, a moment was induced by applying a horizontal load to the loading tower at a given height of impact. The horizontal load was applied through steel wire and a hydraulic cylinder. The height of impact was $h = 11.6$ m. A vertical load was applied that included the self-weight of the foundation, measurement equipment, and loading tower (44.7 kN). A field test demonstrated that failure occurred at a rotation of approximately 2°.

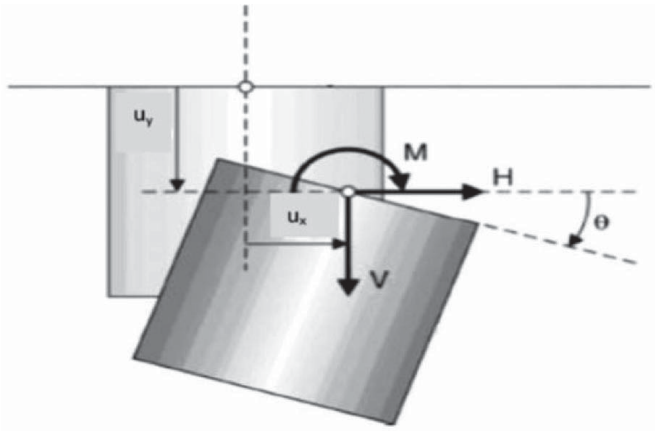

Fig. 3. Sign conventions of loads and displacements used in this study.

Ground Conditions

The sand at the Frederikshavn site consists of fine postglacial marine sand. The sand surrounding the site is a dense, naturally deposited, and undisturbed saturated sand with round-shaped grains. These sand characteristics are reported according to standard classification tests of the Danish code of practice (DGS 2001) and are tabulated in Table 1. The soil characteristics of the Frederikshavn test site are identical to those of Aalborg University sand (Ibsen et al. 2014b).

The effect of degradation due to installation was examined by performing CPT tests prior to, and upon, installation, as shown in Fig. 6. Both the B3 test location and the layout of the CPT samples are shown in Fig. 6. Four CPT samples were collected prior to installation of the bucket, whereas the other samples were collected after installation of the bucket. Special care is given to the data from CPT-1 and CPT-5, which represent the contribution of the disturbance level on the bearing capacity of the suction caissons. High-quality borehole sampling was also completed at the site. For each sample, relative density, water content, unit weight, void ratio, and degree of saturation were determined. Sieve tests were also performed.

Numerical Model

All FEA were conducted by using PLAXIS 3D CE V20 FE software code. Both 10- and 12-node elements were used to model the soil and the interface between the foundation and surrounding soil. The foundation was modeled as a rigid body with a RP prescribed on the centerline at the lid of the foundation.

To choose the domain size of the model, sensitivity analyses were carried out to examine both vertical and shear stresses (σ'_{zz} and σ'_{xz}, respectively). Lateral extension was also examined by tracing the horizontal and shear stresses (σ_{xx} and σ'_{xy}, σ'_{xz}, respectively). The final model was chosen as $(h_m/L) = 6$ and $(L_m/D) = 8$, as outlined in Fig. 7. Mesh refinement of the

(a)

(b)

Fig. 4. (a) Location of the experimental medium-scale model of a monobucket foundation in Frederikshavn (map data ©2021 Google); and (b) bucket foundation used in the offshore tests performed (image by Lars Bo Ibsen).

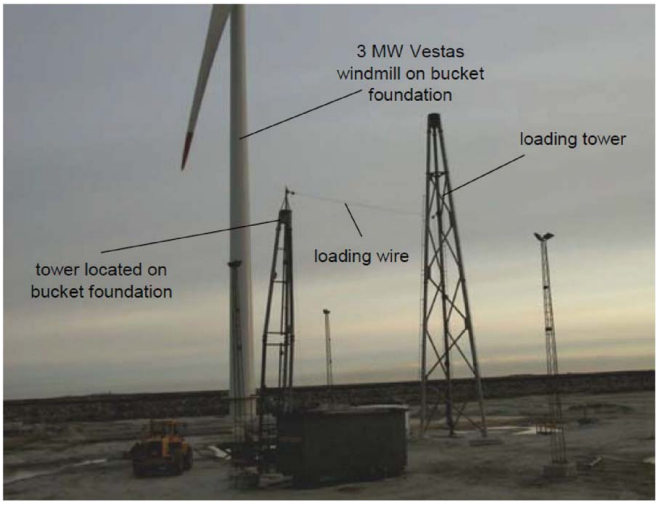

Fig. 5. Loading setup configuration at the Frederikshavn site. (Image by Lars Bo Ibsen.)

Table 1. Sand characteristics given by classification tests

Main grain size, d_{50}	Coefficient of uniformity, $U = d_{60}/d_{10}$	Grain density, G_s	Maximum void ratio, e_{max}	Minimum void ratio, e_{min}
0.16 mm	1.47	2.65	0.962	0.598

Source: Data from Hansson et al. (2005).

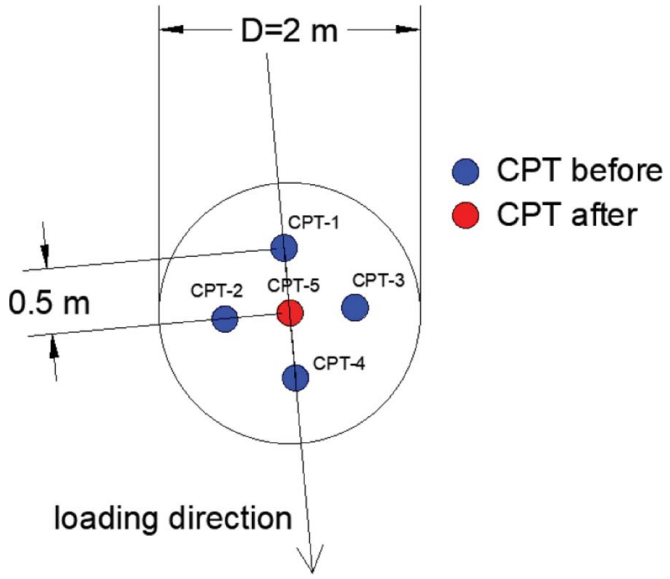

Fig. 6. Location of the CPT tests performed before and after B3 installation.

model consisted of a gradually increasing number of elements around the foundation. A convergence analysis identified 13,433 elements and 22,383 nodes. A realistic assessment was followed, such that a potential numerical overprediction being tolerated if there was merely a minimal improvement but the more elements considered resulted an excessive increase in simulation time. Both horizontal and vertical displacements at the bottom boundary, as well as horizontal displacements at the lateral boundaries, were constrained.

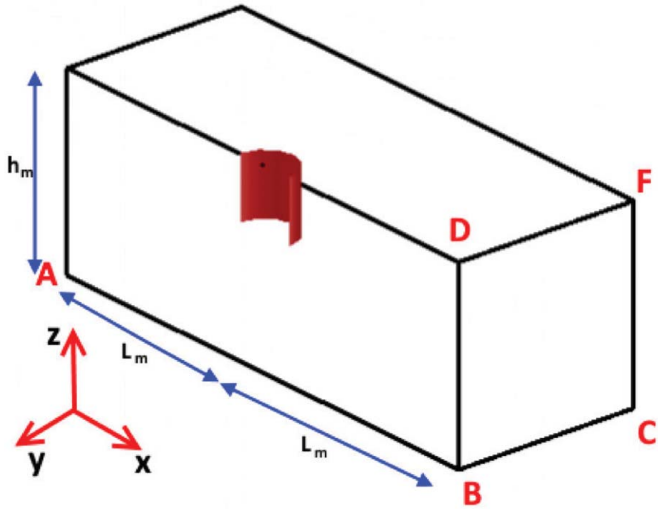

Fig. 7. Dimensions of the FE model.

The FEA was implemented in three stages. First, the soil was subjected to initial stresses induced by geostatic loading. Second, part of the soil was replaced by steel elements. Third, combined loads were applied at the center of the bucket top, including a constant vertical load of 62.22 kN, which represents the weight of the tower and foundation. Concomitantly, the eccentricity-driven loads were monotonically increased until the final load was achieved. The resulting moment was defined by the eccentricity of the horizontal loads from the center of the bucket lid ($h = 19.1$ m).

The constitutive model used to simulate the field test with bucket conducted at the Frederikshavn site is a hardening soil model with small-strain stiffness (HSsmall) (Brinkgreve et al. 2018). This model, in principle, is a modification of the hardening soil (HS) model that accounts for increased stiffness of soils at small strains. Briefly, when strain amplitude increases, soil stiffness decreases nonlinearly. The HSsmall model outlines characteristic shear strains that can be measured proximal to those required to represent geotechnical structures, and it is also applicable to the strain ranges of laboratory tests. The model allows that at minimum strain (which can be measured in both triaxial and oedometer laboratory tests), soil stiffness can be decreased up to half its initial value. The model also allows for very small-strain soil stiffness and its nonlinear dependency.

Under primary triaxial loading conditions, the axial strain, ε_1, and the deviatoric stress, q, are assumed to follow a hyperbolic relationship as given in the following equation:

$$-\varepsilon_1 = \frac{1}{E_i}\frac{q}{1 - q/q_a} \tag{4}$$

where ε_1 = axial strain; E_i = initial stiffness; q = deviatoric stress; and q_a = asymptotic value of shear strength. The initial stiffness, E_i, is related to the secant stiffness, E_{50}, defined at half the value of the deviatoric stress at failure, q_f, by

$$E_i = \frac{2E_{50}}{2 - R_f} \tag{5}$$

where R_f = failure ratio given by q_f/q_a.

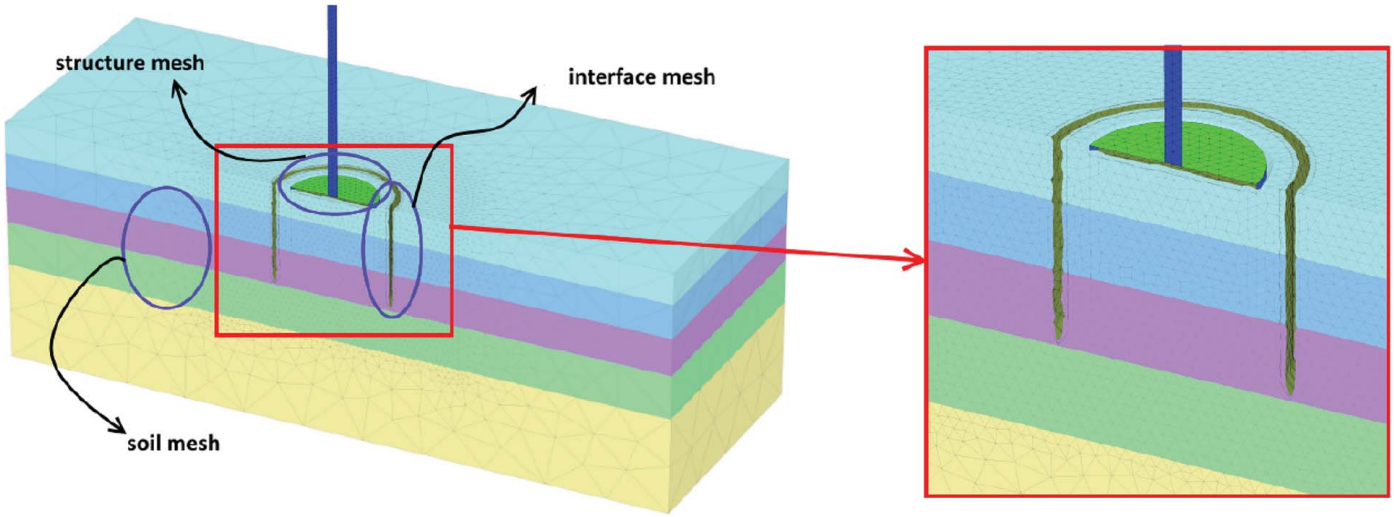

Fig. 8. Final model geometry and mesh fineness for the suction caisson.

Interface

The interface strength reduction factor for the contact elements between the structure and the surrounding area is defined by R_{inter}. This factor controls the stiffness and strength parameters in the interface and is defined by the following equation:

$$R_{\text{inter}} = \frac{\tan(\delta)}{\tan(\varphi)} \tag{6}$$

where $\delta = k\varphi$. Nonetheless, high peaks in stress and strain can appear at the tip of bucket skirts due to abrupt geometry (nonmeaningful jumps in stresses and strains), potentially generating numerical instabilities. This consideration is beyond the interest of the current study, and hence, extended interface elements were introduced according to the recommendation of Østergaard et al. (2013). Thus, both extended vertical and horizontal interfaces up to $0.2D$ below the tip and around the bucket are recommended. The final mesh discretization used is shown in Fig. 8.

Model Calibration for the Frederikshavn Sand

The HS model uses 16 input parameters, of which six are strength and stiffness parameters. The strength parameters are effective friction angle (ϕ'), dilatancy angle (ψ), and effective cohesion (c'). The three stiffness terms are triaxial secant modulus (E_{50}), unloading/reloading stiffness modulus (E_{ur}), and oedometer stiffness modulus (E_{oed}).

A brief overview of the calibration process is given here, with a focus on the parameters defining the strength and stiffness of the layered soil at the given site. This comprised a set of CPTs representing wished-in-place (i.e., the installation effects were not modeled) and installation impact as well as the result of a field test on medium-scale suction bucket foundation.

For this study, the relative density (D_r) and associated effective friction angle (ϕ') were considered primary factors. They were initially calibrated by using CPT test data obtained at the Frederikshavn site.

With particular emphasis on a consistent interpretation of the soil data determined from available field information, CPT-based penetration resistances were adopted to identify relative densities according to empirical expressions detailed in Baldi et al. (1986) and Jamiolkowski et al. (2003) following pioneering work by

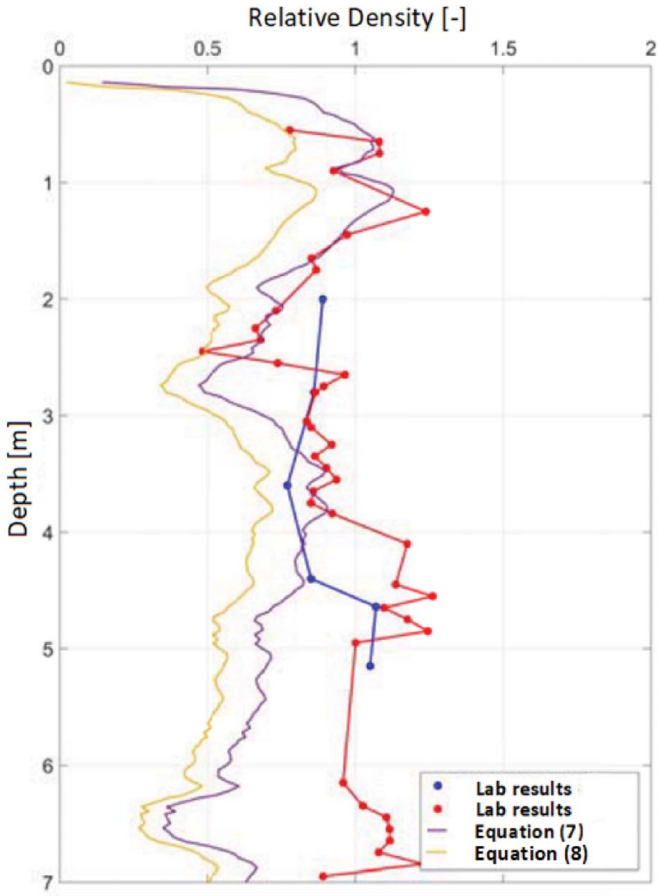

Fig. 9. Comparison of relative density between different theories and laboratory results.

Schmertmann (1976). In terms of soil properties, the original postulate considered normally consolidated (NC) fine to medium, unaged, clean sand and was adopted on the basis of CPTs performed in a calibration chamber (CC). The influence of grain shape and crushability, particularly in the case of siliceous sands, plays a critical role. However, their effect on penetration resistance had been fundamentally overlooked (Lunne et al. 1997). According to Jamiolkowski et al. (1988), CC-based correlation leads to an

Table 2. Values of soil friction angles as derived by employing various methods

	ϕ (°) according to the relative density expression by Jamiolkowski et al. (2003) before installation: CPT-1			ϕ (°) according to the relative density expression by Jamiolkowski et al. (2003) accounting for installation effect: CPT-5		
Depth (m)	Mayne (2006)	Bolton (1986)	Schmertmann (1978)	Mayne (2006)	Bolton (1986)	Schmertmann (1978)
0.02–0.78	42.13	48.62	51.93	37.20	41.62	48.09
0.78–1.62	42.86	50.58	47.86	40.01	44.93	44.41
1.62–2.54	41.59	48.27	44.64	39.05	43.23	41.69
2.54–3.62	40.35	45.96	42.07	36.11	37.56	37.33

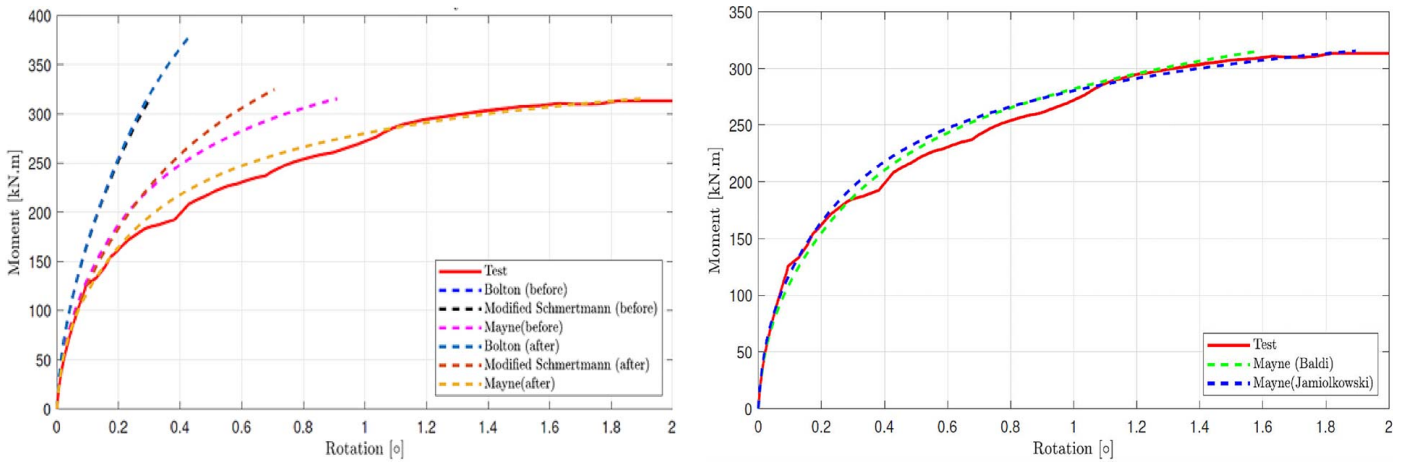

Fig. 10. Validation of FE simulations (wished-in-place as well as those according to suction installation effect) with respect to large-scale experimental results.

Table 3. Final calibrated monobucket according to the HSsmall model and CPT-5 data

Layer parameters	Layer 1	Layer 2	Layer 3	Layer 4
Depth (m)	0–0.78	0.78–1.62	1.62–2.54	2.54–3.62
Thickness (m)	0.78	0.84	0.92	1.08
e_{min}	0.62	0.59	0.56	0.57
e_{int}	0.67	0.64	0.64	0.58
e_{max}	0.89	0.86	0.77	0.85
γ_{dry} (kN/m^3)	15.55	15.84	15.84	16.43
γ_{sat} (kN/m^3)	17.81	18.11	18.52	18.54
φ(°)	37.20	40.00	39.00	36.10
E_{50}^{ref} (MPa)	57.66	75.39	64.87	44.69
E_{oed}^{ref} (MPa)	44.07	52.31	47.57	37.07
E_{ur}^{ref} (MPa)	172.99	226.18	194.6	134.06
G_0^{ref} (MPa)	139.74	168.06	153.02	122.82

underestimation of D_r in the case of sand deposits containing more than 5%–10% fine material.

In light of these considerations, the relative density derived from CPTs is expressed in Eqs. (7) and (8) according to Baldi et al. (1986) and Jamiolkowski et al. (2003), respectively, as follows:

$$D_r = \frac{1}{2.41}\ln\left[\frac{q_t}{157\sigma_{v0}'^{0.55}}\right] \tag{7}$$

$$D_r = \frac{1}{2.96}\ln\left[\left(\frac{q_t}{p_{atm}}\right)/\left(24.94\left(\frac{\sigma_{v0}'((1+2k_0)/3)}{p_{atm}}\right)^{0.46}\right)\right] \tag{8}$$

where q_t = corrected cone resistance; σ_{v0}' = effective overburden pressure; and p_{atm} = atmospheric pressure set to 101.3 kPa.

Meanwhile, the effective friction angles are computed as follows (Mayne 2006; Bolton 1986; Schmertmann 1978):

$$\varphi_{tr}' = 17.6 + 11\log A(q_{t1}) \tag{9}$$

$$\varphi_{tr}' = \varphi_{crit}' - \Delta\varphi_1 - 3D_r + 3I_R \tag{10}$$

$$\varphi_s = 0.146I_D + 41\sigma_3'^{-0.0714} - 1.78 \tag{11}$$

where $q_{t1} = \left((q_t/P_{atm})/\sqrt{(\sigma_{v0}'/P_{atm})}\right)$ = stress normalized cone resistance; φ_{crit}' = the critical friction angle; φ_{tr}' = triaxial friction angle; φ_s = secant friction angle; I_R = relative dilatancy index; I_D = relative density; and $\Delta\varphi_1$ = friction angle reduction due to silt content. For 5%–10% silt content, the friction angle reduction is 2.

The parameters in Eq. (10) are found in an iterative process expressed as follows:

1. The earth pressure coefficient $K_0 = (\sigma_{h0}'/\sigma_{v0}')$ is calculated from an empirical relationship proposed by Jaky (1944), which assumed NC sand, and can be represented as follows:

$$K_0 = 1 - \sin(\varphi_{tr}) \tag{12}$$

2. The relative density is obtained according to Baldi et al. (1986) and Jamiolkowski et al. (2003).
3. The relative density index I_R is calculated by Bolton (1986) as follows:

$$I_R = D_r\left(Q_{min} - \ln\left(\frac{\sigma_{v0}}{1\ \text{kPa}}\right)\right) - 1 \tag{13}$$

where parameter Q_{min} ranges from 5.5 to 10. Jensen (2013) suggested a relative dilatancy index $I_R > 4$ if no laboratory test is conducted.

Lastly, a set of relative density traces, D_r, from CPT and laboratory tests conducted at the location of the selected bucket are

J. Waterway, Port, Coastal, Ocean Eng., 2021, 147(4): 04021008

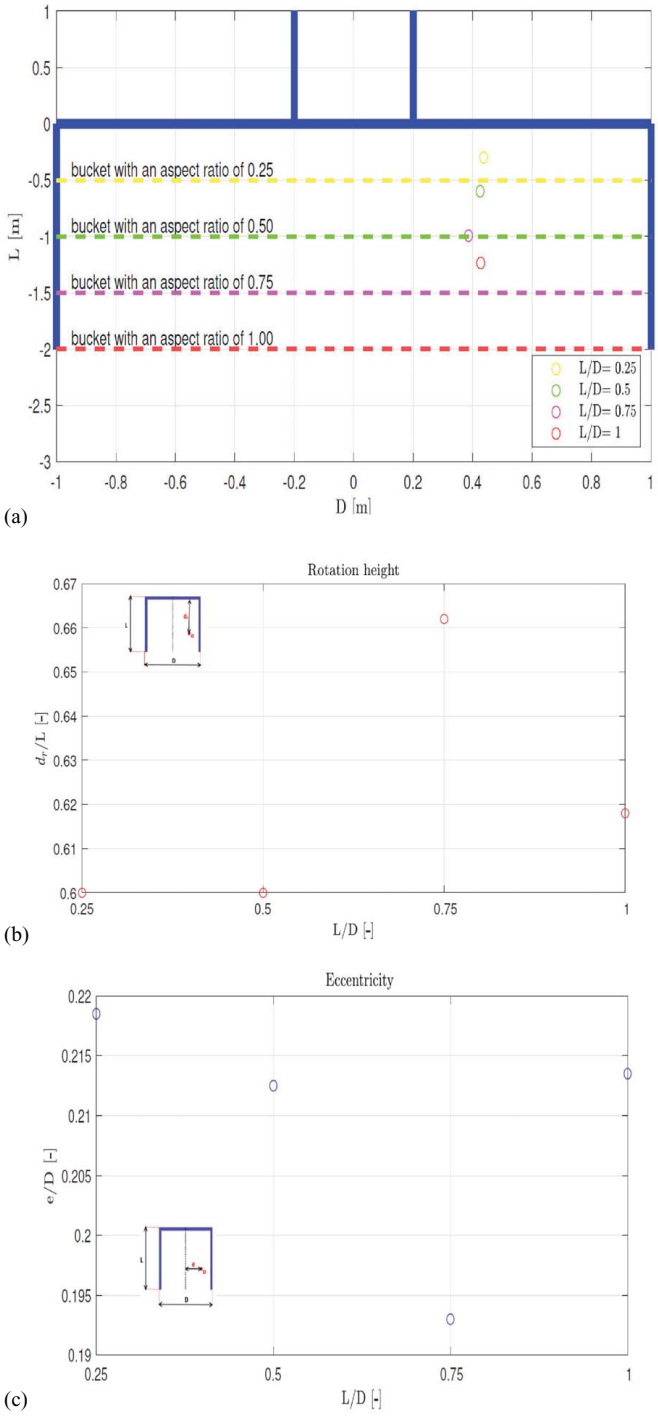

Fig. 11. Trajectory of the rotation center with increasing embedment ratio upon failure. The dashed lines represent the limits of the bucket corresponding to its aspect ratio.

shown in Fig. 9. The traces are reasonably consistent and they confirm the existence of a sand layer at a depth of approximately 7 m across the Frederikshavn test site. Only 3.62 m of this layer is considered for the numerical simulations performed. The soil friction angles obtained from relative densities given by the expression of Jamiolkowski et al. (2003) are considered for further studies and summarized in Table 2.

The other 15 input parameters (here taken as secondary parameters) can either remain at their default values (which are functions of the index property) if no other information is available or can be calibrated to the desired response based on the available load–displacement field test data.

Comparison of Simulation and Physical Test Results

Fig. 10 compares the moment–rotation diagram generated from Test B3 in Basin 4 in layered soil to the moment–rotation diagrams computed by using soil strength parameters following suction installation. The friction angle values for deteriorated soil upon installation are observed to range from 36° to 40° over the depth. Fig. 10 also provides predictions for an undisturbed soil profile (i.e., Class A predictions), capturing the wished-in-place type of analysis, which show a stiffer response than those from the Class A1 predictions (those accounting for installation effect). The terms *before* and *after* in Fig. 10 indicate the friction angles representing the intact soil and disturbed soil, respectively.

Dips in the observed stiffness response align with the degradation in shear strength due to local liquefaction, and they also exhibit excellent agreement with the friction angles given by Mayne (2006). Thus, the A1 prediction is more consistent with Jamiolkowski's expression-compatible calibration, whereas certain discrepancies are observed for the Class A strength values. Once friction angle values have been selected, other input parameters can be calibrated to arrive at a desired bearing strength envelope. Table 3 lists the final calibration parameters used for the field test. Thus, the basis for calibration was the Class A1 prediction, and the other predictions are not included for the sake of brevity.

Taking soil heterogeneity into account, Fig. 11 demonstrates the effects of aspect ratio on the rotation center position. It was confirmed that the rotation center is neither below the skirt tip nor along the centerline [i.e., contrary to solid embedded foundations (Bransby and Yun 2009)]. Rather, the rotation center is observed to deviate from the centerline of the monobucket [i.e., *e* in Fig. 11(c)] in a limit state ranging from approximately 0.19 to approximately 0.22 times the outer diameter. The rotation center eventually tends to approach a stable and consistent position at a rotation angle of 2°. The rotation center positions that are in an approximately identical distance from the centerline are clearly shown in Fig. 11(c). The results agree well with the

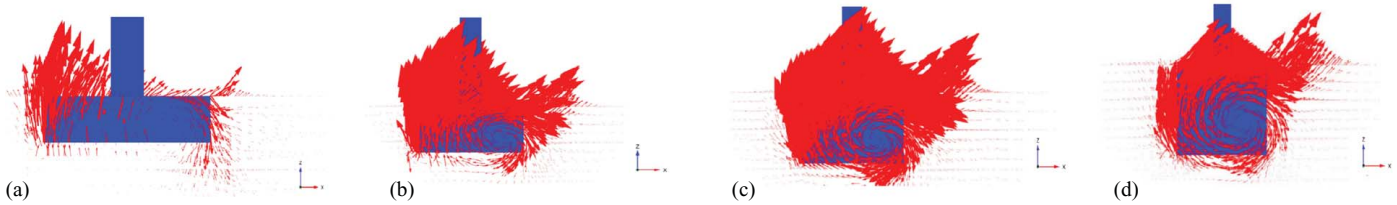

Fig. 12. Comparison of the failure mechanisms (shown as total displacement vectors) that were developed under combined loading in the Frederikshavn field tests when aspect ratios were varied as follows: (a) 0.25; (b) 0.5; (c) 0.75; and (d) 1.

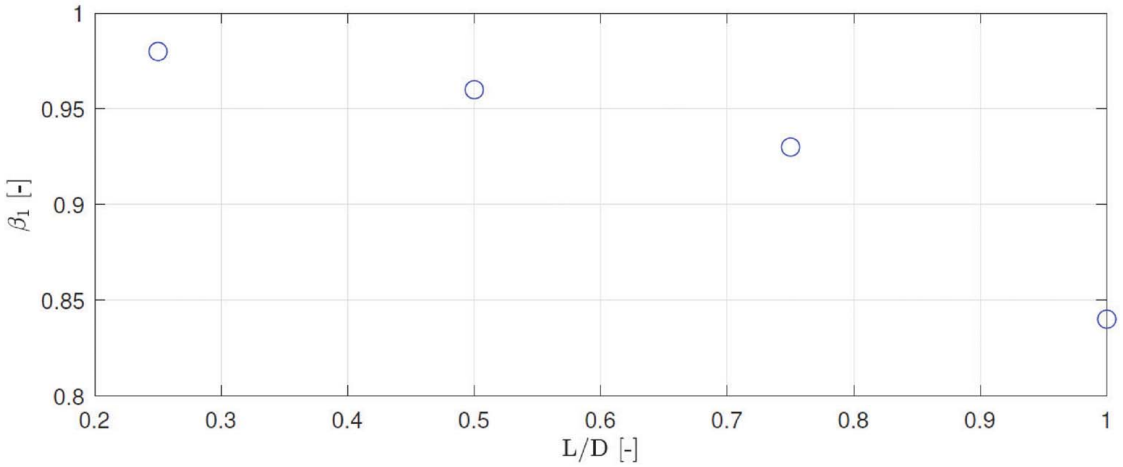

Fig. 13. Calibrated values of β_1 reported by Ibsen et al. (2014b).

Table 4. Vertical and pullout capacities for the case histories examined

L/D	V_{peak} (kN)	V_t (kN)
1	1,600	−276
0.75	1,480	−168.5
0.5	1,340	−81.8
0.25	1,200	−22.5

findings of Li et al. (2015), which considered the bearing capacities of modified suction caissons (MSCs) in single marine fine sand deposits. This observation is most likely due to compliance between the failure mechanisms developing in deformable soil that do not change abruptly between single or multilayered sand deposits.

The vertical distance of rotation point from lid, d_r, for aspect ratios with $L/D \leq 0.5$ was found to be located 0.6 L below the seabed [Fig. 11(b)]. Meanwhile, for aspect ratios with $L/D > 0.5$, the point of rotation is found to move downward [Fig. 11(b)]. These results may be ascribed to a failure mechanism, which consists of an active and passive wedge and a circular shear plane inside the caisson, which is further enhanced as the skirt length decreases. The failure mechanisms depicted in Fig. 12, despite clear differences in soil strata, correspond well with laboratory tests conducted by Liu et al. (2017). In addition, our tests identified that the point of rotation for aspect ratios with $L/D \geq 0.5$ are located 0.7 L below seabed.

Failure Criteria in the *H–M* Plane

To obtain failure criteria for a given suction bucket, failure envelopes were constructed in the *H–M* load space by interpolating between individual *HD/M* load paths identified during a load-controlled analysis. Briefly, a horizontal load was applied and increased until failure occurred. Strictly speaking, a load-controlled analysis procedure is advantageous because the overturning moment capacity can be directly determined for a given set of vertical loading, horizontal loading, moment, and embedment ratio data. Moreover, Taiebat and Carter (2000) previously demonstrated that yield envelopes determined by load-controlled and displacement-controlled approaches are reasonably consistent.

An approximating expression for predicting the shape of *H–M* failure envelopes as a function of a foundation's embedment ratio and soil characteristics is used to fit FE results obtained from various load paths. This expression can be represented as follows:

$$f = \left(\frac{H}{h_0 V_{peak}}\right)^2 + \left(\frac{M}{m_0 D V_{peak}}\right)^2 - 2a\left(\frac{H}{h_0 V_{peak}}\right)\left(\frac{M}{m_0 D V_{peak}}\right) - \left[\frac{\beta_{12}}{(t_0+1)^{(\beta_1+\beta_2)}}\right]\left(\frac{V}{V_{peak}}+t_0\right)^{2\beta_1}\left(1-\frac{V}{V_{peak}}\right)^{2\beta_2} = 0 \tag{14}$$

with t_0 controlling the lower intersection and V_{peak} representing the vertical bearing capacity. Parameters β_1 and β_2 are similar to the curvature factors recommended by Ibsen et al. (2014b); see Fig. 13 for β_1, whereas β_2 is set equal to 1.

The form of Eq. (14) was calibrated by Ibsen et al. (2014a, b) for small-scale model tests, yet it was only defined as a function of embedment ratio because only uniform soil strata were considered in their study.

The prediction was performed twice to evaluate the sensitivity of the failure criteria established by Larsen et al. (2013) and Ibsen et al. (2014a, b) to shift the paradigm to a prototype scale and to account for uncertainties in the soil properties, stress state, foundation geometry, and other factors. The primary goal and emphasis of the calibration undertaken here were to bracket the range of expected responses and to examine whether the adopted failure criteria and calibration protocols can envelop the responses obtained with reasonable allowance for uncertainties.

A crucial parameter with regard to skirted foundation behavior is tensile capacity (V_t), which is presented in a normalized form denoted by t_0. The latter term varies with the ratio of bucket diameter to skirt thickness and can be determined from the following equation:

$$t_0 = -\frac{V_t}{V_{peak}} \tag{15}$$

Numerical simulations and spreadsheet calculations were also performed for a reference system to obtain pure vertical capacity (V_{peak}) and tensile capacity (V_t). The results obtained are presented in Table 4 as a function of the aspect ratio. Tensile capacity was determined from Eq. (16), which takes into account stresses near the skirt. These stresses are reduced due to frictional forces when the

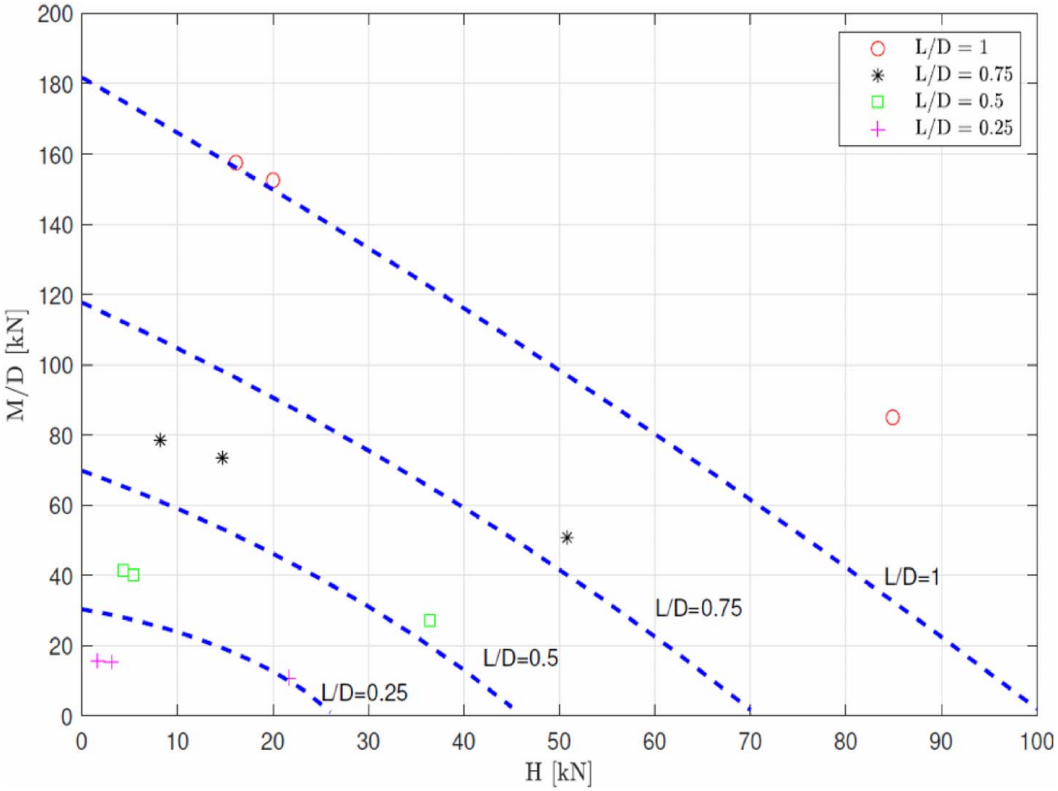

Fig. 14. Bearing strength surface for a given caisson, with $L/D = 0.25$, 0.5, 0.75, or 1 at $\upsilon = 0.5$ considering $\kappa\tan\delta = 2$ as calculated from (1) FE load-based analysis colored dots; and (2) failure envelopes given by Eq. (13).

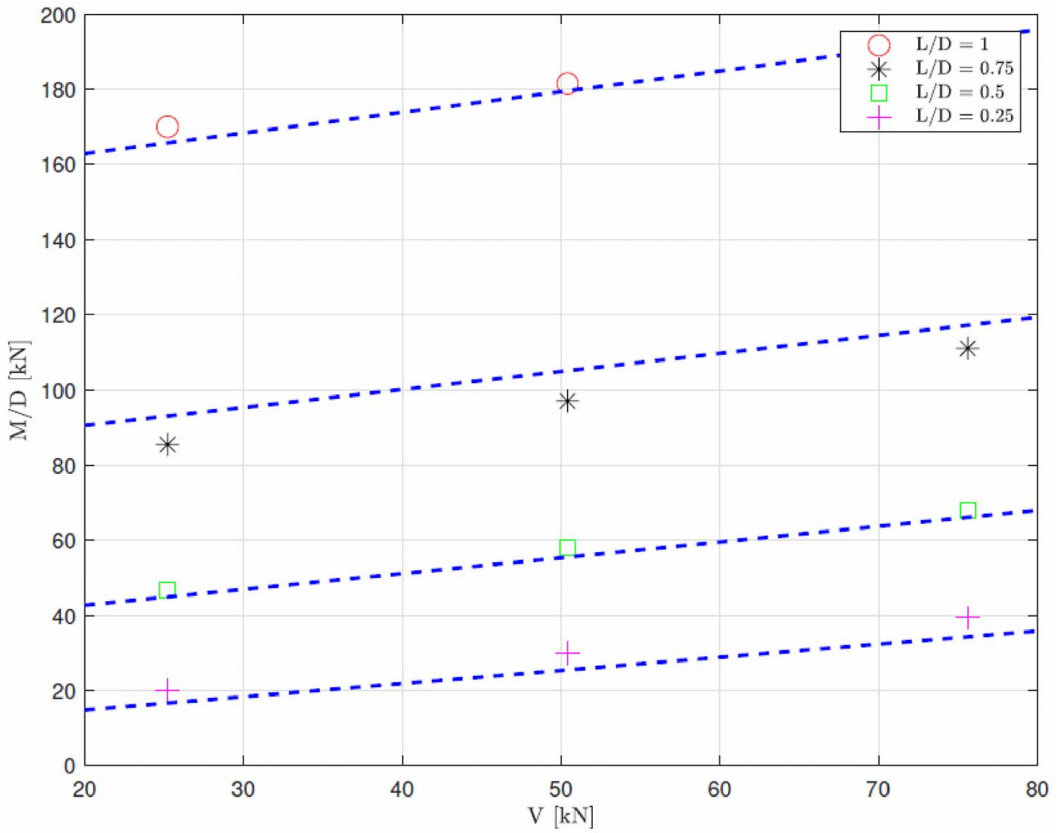

Fig. 15. Comparison of failure criteria and simulation results for low vertical load level, a height of impact of 19.1 m, and various aspect ratios ($L/D =$ 0.25, 0.5, 0.75, and 1).

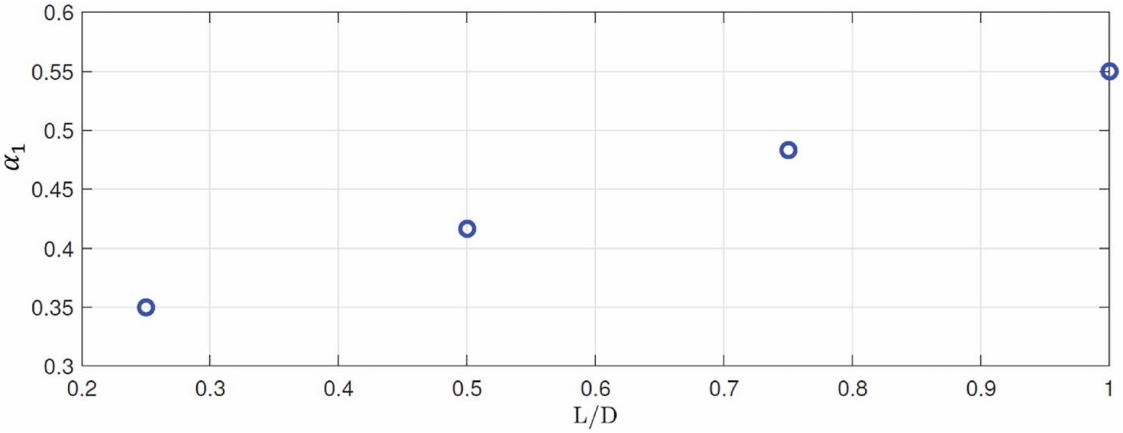

Fig. 16. Inclination factor for determining moment capacity under a low vertical load level.

Table 5. Bearing capacity factors used in this study

L/D	h (m)	K (–)	f_1 (–)	f_2 (–)	α
0.25	19.1	9.55	0.28	0.2685	0.35
0.5	19.1	9.55	0.28	0.2685	0.42
0.75	19.1	9.55	0.28	0.2685	0.48
1	19.1	9.55	0.28	0.2685	0.55

bucket is subjected to a vertical load (Larsen et al. 2013):

$$V_t = -\gamma' Z_o Y_o \left(\frac{h}{Z_o}\right)(k\tan\delta)_o(\pi D_o) - \gamma' Z_i Y_i \left(\frac{h}{Z_i}\right)(k\tan\delta)_i(\pi D_i) \tag{16}$$

where γ' = effective density of the soil; Z_o, Z_i, Y_o, and Y_i = constant parameters; k = lateral earth pressure coefficient; δ = friction angle between the skirt and the soil; and D_o, D_i = outer and inner bucket diameters, respectively.

The parameters, Z_o, Z_i, Y_o, and Y_i, can be determined by using the following equation:

$$Z_i = \frac{D_i}{4(\kappa\tan\delta)_i}$$
$$Z_o = \frac{D_o(m^2-1)}{4(\kappa\tan\delta)_o}$$
$$Y\left(\frac{h}{Z}\right) = \exp\left\{-\left(\frac{h}{Z}\right)\right\} - 1 + \frac{h}{Z} \tag{17}$$

where m = distance over which the stresses are reduced outside the foundation relative to the outer diameter; and h = penetration depth. The parameters, m and $\kappa\tan\delta$, are assumed to be consistent with Larsen et al. (2013).

Fig. 14 compares FEA results from the Class A1 prediction with an approximating expression for selected values of the foundation embedment ratio under operational vertical loads in the radial plane. It is immediately apparent that FEA captures the changing size of the failure envelopes. Intuitively, the envelopes were normalized by dividing the vertical coordinate axis by the diameter, as shown in Fig. 14.

The fitting parameters, h_0, m_0, and a, can then be interpolated to obtain intermediate values of the foundation embedment ratio and may be given by

$$h_0 = 0.032\left(\frac{L}{D}\right)^2 + 0.032\left(\frac{L}{D}\right) + 0.011 \tag{18}$$

$$m_0 = 0.064\left(\frac{L}{D}\right)^2 + 0.067\left(\frac{L}{D}\right) + 0.004 \tag{19}$$

$$a = -15.4\left(\frac{L}{D}\right)^3 + 27.7\left(\frac{L}{D}\right)^2 - 15.1\left(\frac{L}{D}\right) + 2 \tag{20}$$

Based on observational data, the appropriateness of the approximating expressions for the H–M failure envelopes of skirted foundations is validated. Alternative failure surface parameters have also been found to provide a nearly satisfactory match for layered North Sea marine deposits and medium-scale field tests.

Subsequently, Fig. 15 shows two-dimensional slices in the V–M plane with a simplified form of failure envelopes given by Larsen et al. (2013). These failure envelopes are relevant for cases of low vertical load level = V/V_{ult}, by neglecting the scale effect. In addition, the failure envelopes reasonably capture changes in shape that are associated with the foundation embedment ratio.

As expected, the figure shows that moment bearing capacity decreases when the aspect ratio decreases. The results were fitted by using the following equation:

$$\frac{M}{D} = \alpha_1(V - V_t) \tag{21}$$

Determination of failure surface α_1 is shown in Fig. 16, where a linear relationship between the aspect ratio and α_1 is clearly observed.

The nondefault parameters for Class A1 validation involving f_1, f_2, and α are also tabulated in Table 5 with four aspect ratios. They appear to be consistent with those reported by Larsen et al. (2013). It should be noted that h, representing level arm height, is assumed to be constant in order to be compatible with the conditions of the field test. The original data utilized to develop the macroelement model were obtained from tests performed between approximately 0 and 1,000 N, whereas the current model is based on vertical load levels ranging from approximately 20 to 80 kN. Nevertheless, these fitting data provide a reasonably good calibration basis, and this supports their relevance for large-scale caissons.

Explicit Failure Criteria According to Performance of Full-Scale Suction Bucket

At first sight, the equations described previously appear to be based on models containing forms of complexities that are likely to be simplified in the first quadrant of load space. In addition, Eqs. (14) and (21) depend on several failure surface parameters. Alternatively, caisson system behavior is subsequently represented by a particular oblique-shaped parabola.

Hence, a series of FE simulations were performed on a suction bucket with diameters (D) of 12 and 16 m. Eccentricity ratios of horizontal loads for combined loading were varied with $h = 0$, 3, 5, 7, 10, 20, 40, 70, and 100 m. The embedment ratio, L/D, also varied (i.e., 0.25, 0.5, 0.75, and 1), whereas D was kept constant at 12 and 16 m for all of the analyses performed. The skirt thickness of the foundation (t) was set as 40 mm, which is a common thickness for steel buckets. The soil-skirt roughness was set to 0.7 and the mesh elements were first order with 15-node triangular elements. A top plate with a thickness of 0.10 m, a unit weight of 77 kN/m^3, and a very large modulus of elasticity were used for the bucket lid. The bearing capacity was obtained at the intersection point of two tangential lines along the initial and latter portions of the load–deformation curve.

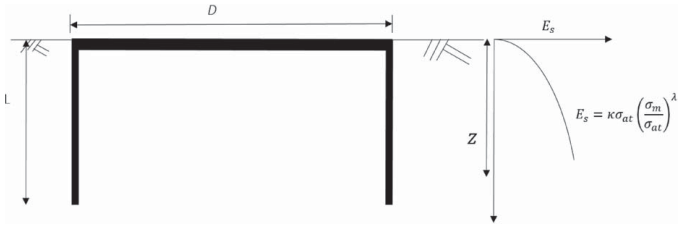

Fig. 17. Foundation geometry and soil conditions.

Table 6. Input properties for E_s

Type	κ	λ	E_s
Loose sand	300	0.65	$1{,}500\sigma_m^{0.65}$
Medium-dense sand	400	0.6	$2{,}524\sigma_m^{0.6}$
Dense sand	600	0.55	$4{,}766\sigma_m^{0.55}$

The oedometric modulus, E_s, was assumed to vary parabolically with depth:

$$E_s = \kappa\sigma_{at}\left(\frac{\sigma_m}{\sigma_{at}}\right)^{\lambda} \tag{22}$$

where $\sigma_{at} = 100$ kN/m^2 is reference stress; σ_m = current mean normal stress in the related soil; and κ and λ = soil stiffness parameters at the reference stress, as shown in Fig. 17 and tabulated in Table 6.

Oblique Parabolalike Failure Envelopes in the H–M *Plane*

Introducing an ellipsoid form of the general behavior in H–M space at a particular vertical load level gives (Zafeirakos and Gerolymos 2016)

$$f = \left(\frac{H}{H_u}\right)^{n_1} + \left(\frac{M}{M_u}\right)^{n_2} + n_3\left(\frac{H}{H_u}\right)\left(\frac{M}{M_u}\right) - 1 = 0 \tag{23}$$

where the coefficients n_1, n_2, and n_3 vary with L/D, υ, and site characteristics.

Recent studies on embedded foundations suggest that the yield function can be expressed in terms of an oblique parabola in H–M space by assuming $n_1 = n_2 = 2$ as follows:

$$f = \left(\frac{H}{H_u}\right)^{2} + \left(\frac{M}{M_u}\right)^{2} + n_3\left(\frac{H}{H_u}\right)\left(\frac{M}{M_u}\right) - 1 = 0 \tag{24}$$

where n_3 = parameter that controls the shape of the surface.

In general, the adopted macroelement model includes different features, and each of the components is considered separately in the following.

Fig. 18 presents limit states under combined horizontal load and moment in the presence of a 10 MN vertical load. These limit states are described with dimensionless geometry measures. An enormous alteration of actual capacity is directly observed as a function of foundation geometry and soil strength profiles.

Kinematic Failure Mechanisms

Up to this point, it has been implicitly demonstrated how both aspect ratio and soil conditions can affect the response of skirted foundations. Moreover, the effect of strength heterogeneity is obvious from the comparisons of obtained data. Embedment and soil stress-dependent stiffness have the greatest influence on the

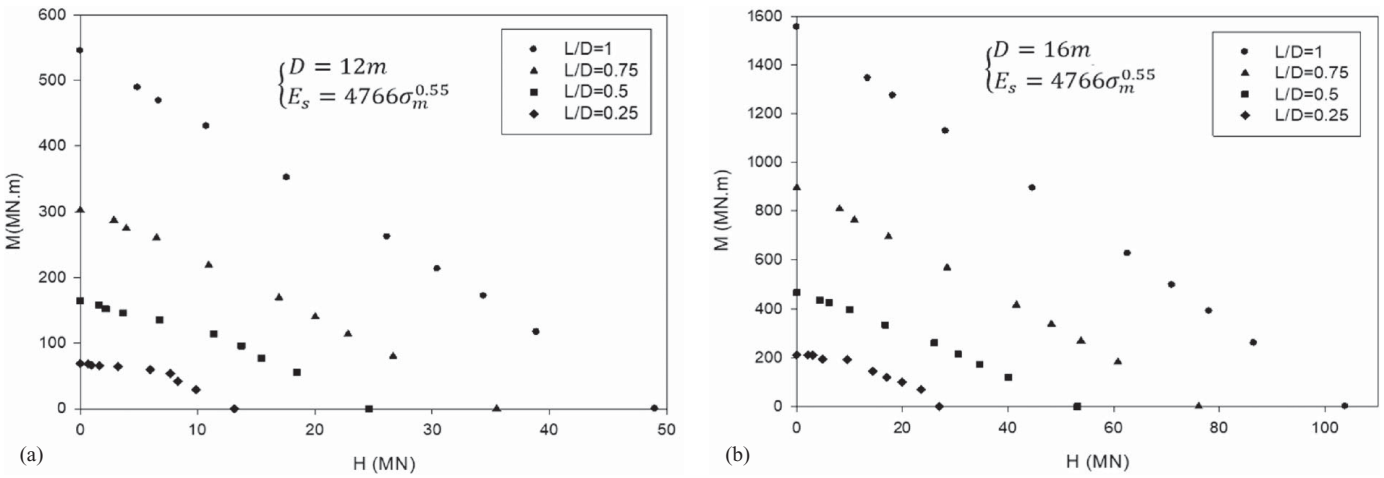

Fig. 18. Failure envelopes in the H–M load plane are shown at different aspect ratios for various sand profiles: (a) $D = 12$ m; and (b) $D = 16$ m.

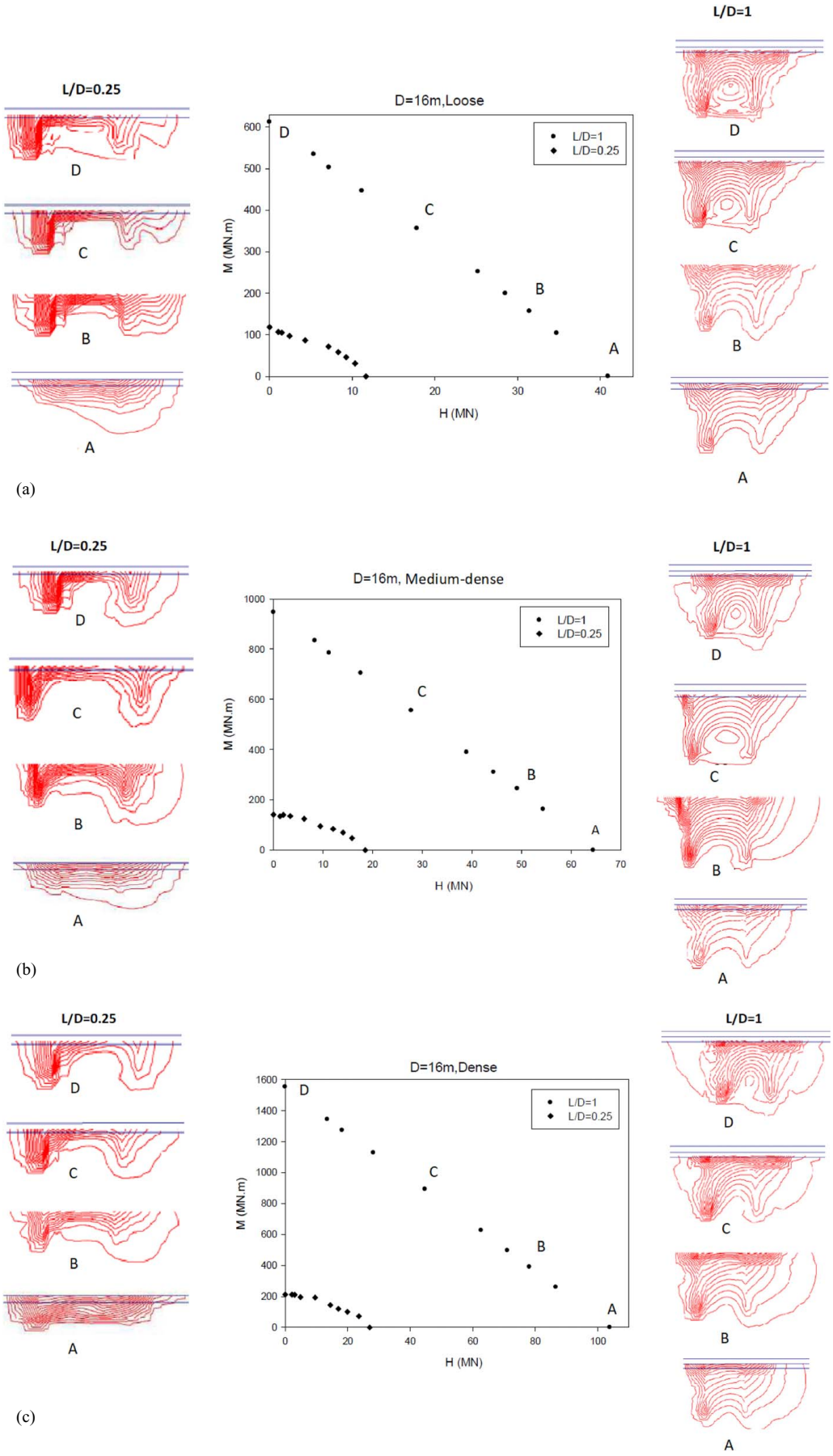

Fig. 19. M–H failure envelopes together with displacement mechanisms calculated with FEA ($V = 10$ MN): (a) $E_s = 1{,}500\sigma_m^{0.65}$; (b) $E_s = 2{,}524\sigma_m^{0.6}$; and (c) $E_s = 4{,}766\sigma_m^{0.55}$.

J. Waterway, Port, Coastal, Ocean Eng., 2021, 147(4): 04021008

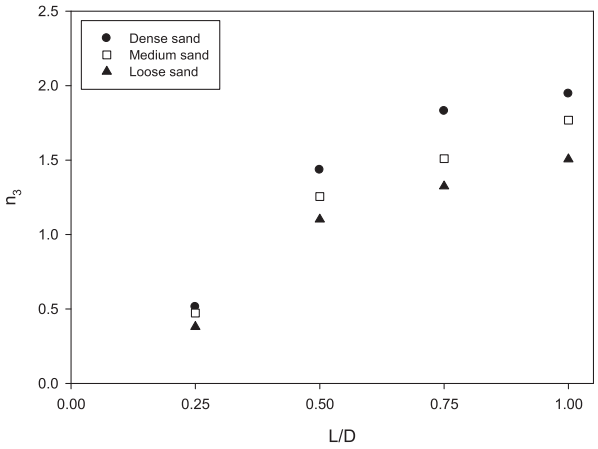

Fig. 20. Values of n_3 for sands with different relative densities versus L/D.

Table 7. n_3 values related to Eq. (24) for different soil strength profiles

Aspect ratio	n_3 values		
L/D	$E_s = 1{,}500\sigma_m^{0.65}$	$E_s = 2{,}524\sigma_m^{0.6}$	$E_s = 4{,}766\sigma_m^{0.55}$
0.25	0.3	0.4	0.5
0.5	1.1	1.2	1.4
0.75	1.3	1.5	1.8
1	1.5	1.7	1.9

shape and size of failure envelopes. Bucket diameter is a secondary influence, and it is not further considered here. The difference in capacity is explained by differences in the soil stiffness profiles and associated changes in deformation mechanisms.

Failure mechanisms for $L/D = 0.25$ and $L/D = 1$ are shown as incremental displacement vectors, which accompany failure in Fig. 19. Points A, B, C, and D on the failure envelope exhibit increasing ratios of M/H for a given foundation. The mechanisms at A correspond to pure horizontal capacity, H_{ult}, upon which the scoop mechanism prevails with enhanced rotation in the anticlockwise direction for the deeper foundation. This effect is less obvious for shallower caissons. For the latter, the foundation considerably displaces the most upfront and back surrounding soil instead of mobilizing the scoop scheme. In particular, the translation mechanism may be dominant for $E_s = 4{,}766\sigma_m^{0.55}$, which is representative of denser soil. However, the extent of sliding is clearly dependent on strength heterogeneity according to the soil strength profile used. The widest amount of sliding is evident from simulations on loose sand.

Fig. 19 also provides an explanation for the different failure envelopes when M/H increases. For these conditions, Points B, C, and D on the failure envelopes mark the transition from a sliding failure mechanism of foundations with lower skirt length (i.e., $L/D = 0.25$) to an exacerbated rotational mode. However, incremental displacement of the vectors illustrates a developing internal mechanism that is involved in almost all cases, irrespective of considerable differences in their strength profiles. For point A at deeper skirts,

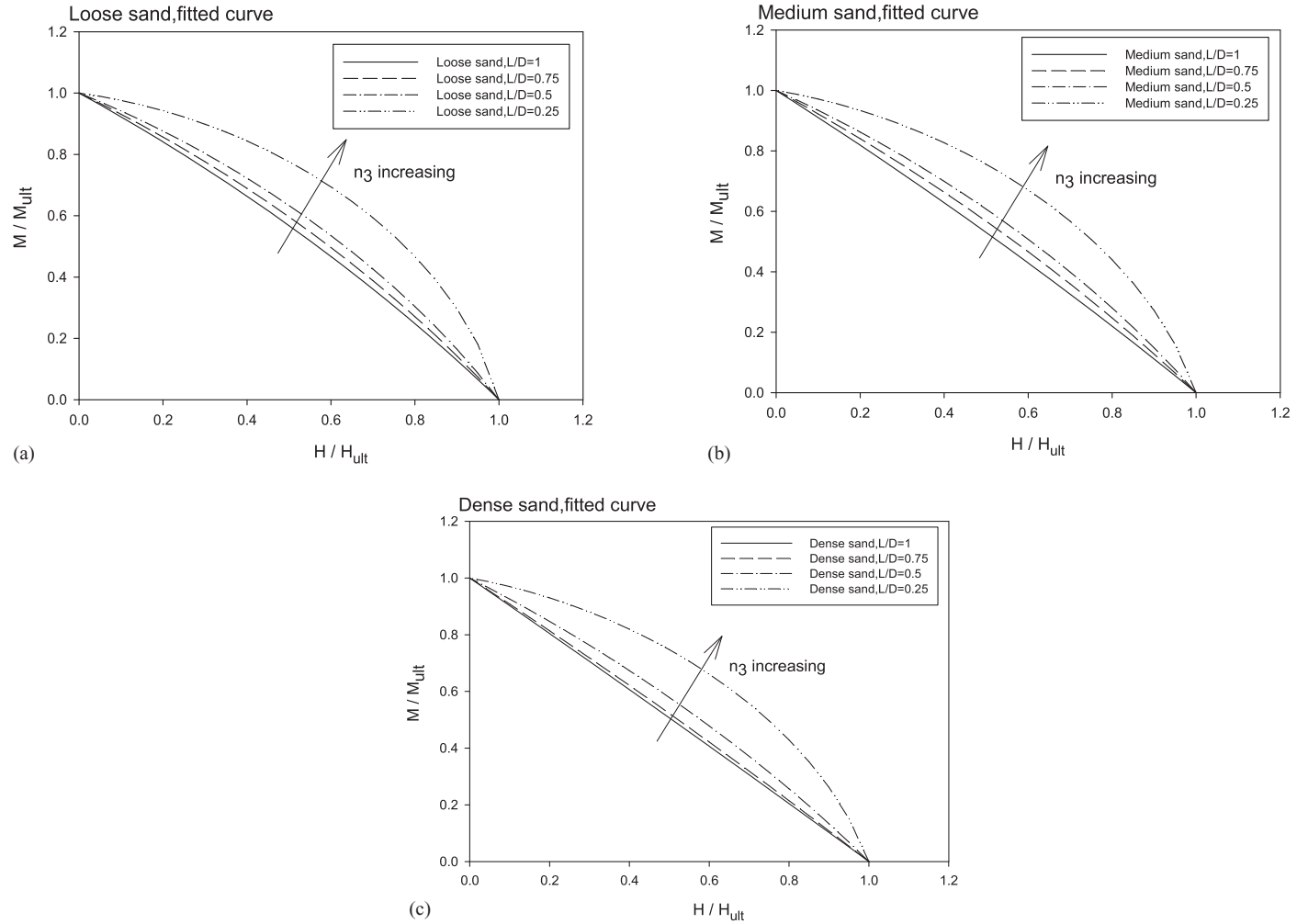

Fig. 21. Expansion of the yield surface with decreasing embedment due to (a) loose sand; (b) medium sand; or (c) dense sand.

J. Waterway, Port, Coastal, Ocean Eng., 2021, 147(4): 04021008

the scoop mechanism prevails at Point D. Despite clear differences between prevailing strengths, deeper foundations would inhibit internal mechanisms from developing within skirts, thereby leading to a reduced bearing capacity level.

Calibration of the Oblique Parabolalike Model

It remains questionable whether the expression presented previously is sufficiently versatile to be applicable to a range of soil strength profiles. By employing a simple approximating expression, generalized failure envelopes for the extensive range of conditions considered are able to be predicted. In addition, bearing capacity factors were determined for different strength profiles as a function of embedment.

To visualize the influence of n_3 on the shape of a strength surface, additional numerical analyses were performed to accurately predict this parameter, as illustrated in Fig. 20 and Table 7. The factor, n_3, in Eq. (24) can be altered to adjust the shape of the locus to try to fit failure envelopes for sands with different relative densities. Fig. 20 presents the results of least squares regression analyses as n_3 values are varied versus L/D and soil strength profiles. Higher n_3 values are achieved as the embedment ratio and soil strength increase, whereas the positive impact of n_3 on soils with greater stiffness is less obvious at shallow skirt lengths (i.e., $L/D = 0.25$).

Regression analyses for determining n_3 also resulted in the following algebraic functions. The fitting parameters can be interpolated to obtain intermediate values of foundation aspect ratio and soil stiffness:

$$n_3 = 2 - 0.143(L/D)^{-1.698} \quad \text{for } E_s = 4{,}766\sigma_m^{0.55} \tag{25}$$

$$n_3 = 2 - 0.323(L/D)^{-1.126} \quad \text{for } E_s = 2{,}524\sigma_m^{0.6} \tag{26}$$

$$n_3 = 2 - 0.511(L/D)^{-0.831} \quad \text{for } E_s = 1{,}500\sigma_m^{0.65} \tag{27}$$

The aforementioned expressions, which incorporate the effect of parabolic ground profiles, provide a good fit to the FE analyses performed. Moreover, these expressions could be applied to $0.25 \le L/D \le 1$. Fig. 21 illustrates the expansion that failure envelopes undergo with decreasing L/D, as well as the contribution of n_3 to alterations in the failure envelopes. Fig. 22 further demonstrates that the expansion of failure envelope surfaces occurs as the relative density of sands decreases. The influence of n_3 in normalized $(M/M_{ult}) - (H/H_{ult})$ space is also observed at discrete levels of the aspect ratios (Fig. 22). The embedment ratio drastically influences the shape of the failure envelope for suction caissons with a low aspect ratio (i.e., 0.25), consistent with the rapid alterations that occur in the kinematic mechanisms accompanying failure (Fig. 19).

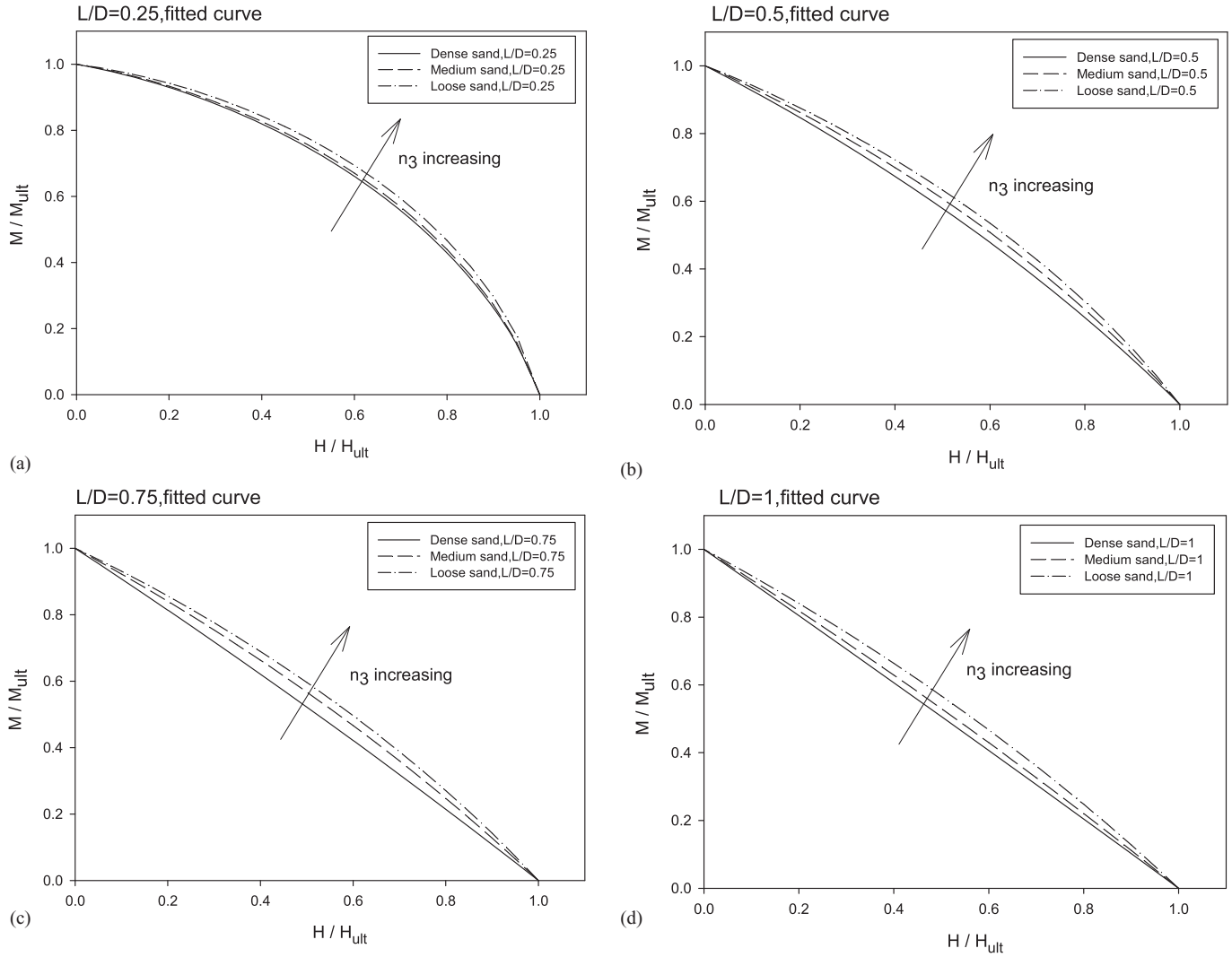

Fig. 22. Expansion of the yield surface with decreasing soil strength profiles: (a) $L/D = 0.25$; (b) $L/D = 0.5$; (c) $L/D = 0.75$; and (d) $L/D = 1$.

J. Waterway, Port, Coastal, Ocean Eng., 2021, 147(4): 04021008

Despite a bit of scattering, Fig. 22 shows that failure envelopes are closely banded for each embedment ratio. In contrast, Fig. 21 illustrates that variances in embedment ratios, irrespective of ground profiles, represent a secondary effect in soil strength profiles.

Concluding Remarks

Here, we present numerical simulations of soil–structure interactions that occur for laterally loaded suction bucket foundations. These simulations validate our numerical modeling approach and provide insights into the current capacity of failure criteria to predict the bearing capacity of skirted foundations. Class A and Class A1 predictions for two cases of undisturbed and disturbed soil conditions, respectively, are performed for a reference foundation installed at the Frederikshavn site. Both sets of results are compared to a recorded B3 test. Rigorous integration of soil data from field investigations is key for performing a robust calibration of the chosen model and, in particular, for addressing degraded soil strength following suction installation. For constitutive soil parameters that had no corresponding data available, these parameters are set to default calibration targets expected for a load–deformation response.

The Class A1 prediction emphasizes the constitutive responses that are most important to the response of a soil–foundation system. As a result, it is observed that the trajectory of the rotation center was altered an identical distance from the caisson centerline with increasing skirt length at failure. For the failure envelopes, the calibration targets the range of expected failure surface parameters, as well as available literature data. On average, the general trends, responses, and existing expressions from the model tests are successfully captured in our numerical simulations, particularly for low vertical load levels. The small scatter that existed is attributed to uncertainty in regard to differences in stress levels between the executed field tests and the scaled model tests (which failure envelopes have originally been deemed for), site characteristics and determination of soil parameters, as well as the heterogeneity of soil strength and stiffness properties within the soil strata.

For Class C simulations, simple algebraic expressions are developed. They explain no unique relationship for the existence of combined failure envelopes due to complex interactions among bucket geometry, soil stiffness heterogeneity, and level of load eccentricity for skirted foundations.

The relative importance of key issues has shown that the shape and size of normalized failure envelopes profoundly vary with the embedment ratio, and to a lesser extent, with stiffness profiles. For structural conditions independent of soil strength and stiffness, the predictions reveal that the addition of skirt length to achieve an embedment ratio greater than 25% significantly alters the shape and size of associated failure envelopes.

Data Availability Statement

Some or all data, models, or code generated or used during the study are available from the corresponding author by request.

Acknowledgments

The authors gratefully acknowledge the financial support received from the European Union's Horizon 2020 research and innovation program under Grant Agreement No. 818153. This study is funded as part of the i4Offshore project (Integrated Implementation of Industrial Innovations for Offshore Wind Cost Reduction).

References

Achmus, M., C. T. Akdag, and K. Thieken. 2013. "Load-bearing behavior of suction bucket foundations in sand." *Appl. Ocean Res.* 43: 157–165. https://doi.org/10.1016/j.apor.2013.09.001.

Baldi, G., V. N. Bellotti, N. Chionna, M. Jamiolkowski, and E. Pasqualini. 1986. "Interpretation of CPT's and CPTU's-2nd part: Drained penetration of sands." In *Proc., 4th Int. Geotechnical Seminar Field Instrumentation and In-Situ Measurements*, 143–156. Singapore: Nanyang Technological Institute.

Barari, A., and L. B. Ibsen. 2012. "Undrained response of bucket foundations to moment loading." *Appl. Ocean Res.* 36: 12–21. https://doi.org/10.1016/j.apor.2012.01.003.

Barari, A., and L. B. Ibsen. 2017. "Insight into the lateral response of offshore shallow foundations." *Ocean Eng.* 144: 203–210. https://doi.org/10.1016/j.oceaneng.2017.08.012.

Bhattacharya, S. 2019. *Design of foundations for offshore wind turbines*. Hoboken, NJ: Wiley.

Bienen, B., C. H. Gaudin, M. Cassidy, L. Rausch, and O. A. Purwana. 2012. "Numerical modeling of undrained capacity of hybrid skirted foundation under combined loading." *Int. J. Offshore Polar Eng.* 22 (4): 323–329.

Bolton, M. D. 1986. "The strength and dilatancy of sands." *Géotechnique* 36 (1): 65–78. https://doi.org/10.1680/geot.1986.36.1.65.

Bransby, M. F., and G. J. Yun. 2009. "The undrained capacity of skirted strip foundations under combined loading." *Géotechnique* 59 (2): 115–125. https://doi.org/10.1680/geot.2007.00098.

Brinkgreve, R. B. J., S. Kumarswamy, and W. M. Swolfs. 2018. *PLAXIS 3d 2018 manual*. Delft, Netherlands: PLAXIS.

Cassidy, M. J. 1999. "Non-linear analysis of jack-up structures subjected to random waves." D.Phil. thesis, New College, Univ. of Oxford.

Cassidy, M. J., B. W. Byrne, and G. T. Houlsby. 2002. "Modelling the behavior of circular footings under combined loading on loose carbonate sand." *Géotechnique* 52 (10): 705–712. https://doi.org/10.1680/geot.2002.52.10.705.

DGS (Danish Geotechnical Society). 2001. *Handbook of laboratory work*. DGF-Bulletin 15. [In Danish.] Lyngby, Denmark: DGS.

Gerolymos, N., A. Zafeirakos, and C. Souliotis. 2012. "Insight to failure mechanisms of caisson foundations under combined loading: A macroelement approach." In *Proc., 2nd Int. Conf. on Performance-Based Design in Earthquake Geotechnical Engineering*, 1–10. Taormina, Italy: ISSMGE.

Gottardi, G., and G. T. Houlsby. 1995. *Model tests of circular footings on sand subjected to combined loads*. Rep. No. OUEL 2071/95. Oxford, UK: Univ. of Oxford.

Gottardi, G., G. T. Houlsby, and R. Butterfield. 1999. "The plastic response of circular footings on sand under general planar loading." *Géotechnique* 49 (4): 453–469. https://doi.org/10.1680/geot.1999.49.4.453.

Gourvenec, S. 2008. "Effect of embedment on the undrained capacity of shallow foundations under general loading." *Géotechnique* 58 (3): 177–185. https://doi.org/10.1680/geot.2008.58.3.177.

Hansson, M., T. H. Hjort, and M. Thaarup. 2005. "Static and transient loading of the bucket foundation." M.Sc. thesis, Dept. of Civil Engineering, Aalborg Univ.

Houlsby, G. T., L. B. Ibsen, and B. W. Byrne. 2005. "Suction caissons for wind turbines." In *Frontiers in Offshore Geotechnics: Int. Symp. on Frontiers in Geotechnics*, edited by S. Gourvenec and M. Cassidy, 75–94. London: Taylor & Francis.

Ibsen, L. B., A. Barari, and K. A. Larsen. 2014a. "Adaptive plasticity model for bucket foundations." *J. Eng. Mech.* 140 (2): 361–373. https://doi.org/10.1061/(ASCE)EM.1943-7889.0000633.

Ibsen, L. B., A. Barari, and K. A. Larsen. 2015. "Effect of embedment on the plastic behavior of bucket foundations." *J. Waterway, Port, Coastal, Ocean Eng.* 141 (6): 06015005. https://doi.org/10.1061/(ASCE)WW.1943-5460.0000284.

Ibsen, L. B., K. A. Larsen, and A. Barari. 2014b. "Calibration of failure criteria for bucket foundations on drained sand under general loading." *J. Geotech. Geoenviron. Eng.* 140 (7): 04014033. https://doi.org/10.1061/(ASCE)GT.1943-5606.0000995.

Jaky, J. 1944. "The coefficient of earth pressure at rest." [In Hungarian.] *J. Soc. Hung. Archit. Eng.* 78 (22): 355–358.

Jamiolkowski, M., V. N. Ghionna, R. Lancellotta, and E. Pasqualini. 1988. "New correlations of penetration tests for design practice." In Vol. 1 of *Penetration Testing 1988, ISOPT 1*, edited by J. De Ruiter, 263–296. Rotterdam, The Netherlands: A. A. Balkema.

Jamiolkowski, M., D. C. L. Presti, and M. Manassero. 2003. "Evaluation of relative density and shear strength of sands from CPT and DMT." In *Soil Behavior and Soft Ground Construction*, Geotechnical Special Publication 119, edited by J. T. Germaine, T. C. Sheahan, and R. V. Whitman, 201–238. Reston, VA: ASCE.

Jensen, B. C. 2013. *Teknisk ståbi 22*. Copenhagen, Denmark: Nyt teknisk forlag.

Larsen, K. A., L. B. Ibsen, and A. Barari. 2013. "Modified expression for the failure criterion of Bucket foundations subjected to combined loading." *Can. Geotech. J.* 50 (12): 1250–1259. https://doi.org/10.1139/cgj-2012-0308.

Li, D., Y. Zhang, L. Feng, and Y. Gao. 2015. "Capacity of modified suction caissons in marine sand under static horizontal loading." *Ocean Eng.* 102: 1–16. https://doi.org/10.1016/j.oceaneng.2015.04.033.

Liu, M., J. Lian, and M. Yang. 2017. "Experimental and numerical studies on lateral bearing capacity of bucket foundation in saturated sand." *Ocean Eng.* 144: 14–20. https://doi.org/10.1016/j.oceaneng.2016.04.001.

Lunne, T., P. K. Robertson, and J. J. M. Powel. 1997. *Cone penetration testing in geotechnical practice*. London: Blackie Academic and Professional.

Mayne, P. W. 2006. "In-situ test calibrations for evaluating soil parameters." In Vol. 3 of *Characterization & Engineering Properties of Natural Soils*, 1602–1652. London: Taylor & Francis.

Østergaard, M. U., B. S. Roesen, and L. B. Ibsen. 2013. "p–y curves for bucket foundations in sand using finite element modeling." In *Proc., 3rd Int. Symp. on Frontiers in Offshore Geotechnics*, 343–348. London: CRC Press.

Schmertmann, J. H. 1976. *An updated correlation between relative density DR and Fugro-type electric cone bearing, qc*. Rep. No. DACW 39-76 M 6646. Vicksburg, MS: WES.

Schmertmann, J. H. 1978. *Guidelines for cone penetration test, performance and design*. Washington, DC: Federal Highway Administration.

Taiebat, H. A., and J. P. Carter. 2000. "Numerical studies of the bearing capacity of shallow foundations on cohesive soils subjected to combined loading." *Géotechnique* 50 (4): 409–418. https://doi.org/10.1680/geot.2000.50.4.409.

Vulpe, C., S. Gourvenec, and M. Power. 2014. "A generalized failure envelope for undrained capacity of circular shallow foundations under general loading." *Géotech. Lett.* 4 (3): 187–196. https://doi.org/10.1680/geolett.14.00010.

Zafeirakos, A., and N. Gerolymos. 2016. "Bearing strength surface for bridge caisson foundations in frictional soil under combined loading." *Acta Geotech.* 11 (5): 1189–1208. https://doi.org/10.1007/s11440-015-0431-7.

Zhu, F., B. Bienen, C. Loughlin, M. J. Casidy, and N. Morgan. 2019. "Suction caisson foundations for offshore wind energy: Cyclic response in sand and sand over clay." *Géotechnique* 69 (10): 924–931. https://doi.org/10.1680/jgeot.17.P.273.